

# Comparing Dynamics, Pinning and Ratchet Effects for Skyrmionium, Skyrmions, and Antiskyrmions

J. C. Bellizotti Souza<sup>1</sup>, N. P. Vizarim<sup>2</sup>, C. J. O. Reichhardt<sup>3</sup>, C. Reichhardt<sup>3</sup>, and P. A. Venegas<sup>4</sup>

E-mail: [jc.souza@unesp.br](mailto:jc.souza@unesp.br)

<sup>1</sup> POSMAT - Programa de Pós-Graduação em Ciência e Tecnologia de Materiais, São Paulo State University (UNESP), School of Sciences, Bauru 17033-360, SP, Brazil

<sup>2</sup> “Gleb Wataghin” Institute of Physics, University of Campinas, 13083-859 Campinas, São Paulo, Brazil

<sup>3</sup> Theoretical Division and Center for Nonlinear Studies, Los Alamos National Laboratory, Los Alamos, New Mexico 87545, USA

<sup>4</sup> Department of Physics, São Paulo State University (UNESP), School of Sciences, Bauru 17033-360, SP, Brazil

## Abstract.

We compare the driven dynamics of skyrmions, antiskyrmions, and skyrmionium interacting with random disorder, circular defects, and asymmetric potentials. When interacting with a line defect at a constant drive, skyrmions and antiskyrmions show an acceleration effect for motion along the wall and a drop in velocity when they can cross the barrier. In contrast, skyrmionium travels at a reduced velocity when moving along a wall, and exhibits an increase in velocity once it can cross the barrier. For point defects, skyrmionium can be pinned for a finite fixed period of time, while for skyrmions and antiskyrmions, the Magnus force creates a deflection from the defect and an acceleration effect. For a given drive, skyrmionium moves twice as fast as skyrmions; however, skyrmionium is more susceptible to pinning effects than skyrmions and antiskyrmions. Additionally, there is a critical threshold where the skyrmionium transforms to a skyrmion that is associated with a drop in the velocity of the texture. We show that all three textures exhibit diode and ratchet effects when interacting with an asymmetric substrate, but skyrmions and antiskyrmions show a stronger ratcheting effect than skyrmionium due to the Magnus force.

## 1. Introduction

Skyrmions are particle like magnetic textures that can occur in chiral magnets and are characterized by their topology [1, 2, 3]. Skyrmions can be set in motion using various techniques [4, 5, 6, 7, 8], and can also interact with defect sites [9, 10, 11, 12, 13, 14, 15] or structured patterns [16, 17, 15]. Due to their size scale, stability, and mobility, they are promising candidates for various applications such as memory devices [18] or novel computing approaches [19, 20]. Due to their topology, skyrmions exhibit strong Magnus effects when compared to other quasi-particles which causes them to deviate by an angle with respect to the applied drive, a phenomenon that is known as the skyrmion Hall effect (SHE) [21, 22, 23, 15]. This Magnus force component in skyrmions significantly affects their dynamical behavior when they interact with pinning sites or obstacles, leading to novel types of transport and motion control [12, 15, 24, 25, 26]. For example, skyrmions can spiral around circular or point defects [27, 28, 15], and can experience acceleration effects [29, 30, 31, 32, 33] upon interacting with line barriers, which provide them with a velocity boost. When skyrmions interact with asymmetric substrates or barriers, they exhibit a diode effect [34, 35, 36, 37, 38] under dc driving or ratchet effects under ac driving [39, 40, 41, 42].

Skyrmions can be characterized by their topological number  $Q = \pm 1$  [3, 40]. There are also additional topological textures, including antiskyrmions [43, 44, 45, 46, 47, 48, 49] with  $Q = \mp 1$ , and skyrmionium [50, 51, 52, 53, 54, 55, 56] with  $Q = 0$ . Since these textures can have different dynamics, it would be valuable to perform a direct comparison of the way the textures interact with different types of defects.

In this work we consider atomistic simulations of skyrmions, antiskyrmions, and skyrmionium to compare their dynamics as they interact with circular, line, and asymmetric barriers. In the case of a line defect, skyrmionium runs along the wall with a reduced net velocity, while at higher drives where the skyrmionium can jump over the line defect, the velocity shows a sharp increase. In contrast, skyrmions and antiskyrmions moving along the wall have a strongly increased velocity, or boost, due to the Magnus force, and when the drive becomes large enough to permit the skyrmions and antiskyrmions to hop over the wall, there is a drop in the velocity when the boost effect is lost. For a fixed drive, the skyrmionium moves twice as fast as the skyrmions and antiskyrmions; however, the skyrmionium is more strongly affected by the pinning. A skyrmionium interacting with circular defects exhibits a velocity reduction and entrance into a temporarily pinned state before moving again. In contrast, the skyrmion and antiskyrmion textures are deflected around the circular defects and show a pronounced velocity boost. When the textures are driven over a random disordered background, skyrmionium has a higher depinning threshold than the skyrmions and antiskyrmions at high anisotropy defect strengths. In the sliding state, the skyrmionium velocity is higher than that of the skyrmions, but above a critical drive the skyrmionium transforms into a skyrmion state, which results in a sudden drop in the velocity. We show that all three textures exhibit diode and ratchet effects when interacting with an asymmetric substrate.

## 2. Methods

Using atomistic simulations [57], we model an ultrathin ferromagnetic film at zero temperature  $T = 0$  K, with periodic boundary conditions along the  $x$  and  $y$  directions. The atomistic dynamics are governed by the Hamiltonian [57, 58, 59]:

$$\mathcal{H} = - \sum_{i,\langle i,j \rangle} J_{ij} \mathbf{m}_i \cdot \mathbf{m}_j - \sum_{i,\langle i,j \rangle} \mathbf{D}_{ij} \cdot (\mathbf{m}_i \times \mathbf{m}_j) - \sum_i \mu \mathbf{H} \cdot \mathbf{m}_i - \sum_i K (\mathbf{m}_i \cdot \hat{\mathbf{z}})^2$$

The ultrathin film is modeled as a square arrangement of atoms with a lattice constant  $a = 0.5$  nm. Here,  $\langle i, j \rangle$  indicates that the sum is over only the first neighbors of the  $i$ th magnetic moment. The first term on the right hand side of Eq. (1) is the exchange interaction with an exchange constant of  $J_{ij} = J$  between magnetic moments  $i$  and  $j$ . The second term is the Dzyaloshinskii–Moriya (DM) interaction. Here, since we are concerned with skyrmionium, skyrmions, and antiskyrmions, the DM vector  $\mathbf{D}_{ij}$  between sites  $i$  and  $j$  differs depending on the choice of texture to be simulated. For skyrmionium and skyrmions, the DM vector is given by the isotropic interfacial vector  $\mathbf{D}_{ij} = D\hat{\mathbf{z}} \times \hat{\mathbf{r}}_{ij}$ , where  $D$  is the DM interaction strength and  $\hat{\mathbf{r}}_{ij}$  the unit distance vector between sites  $i$  and  $j$ . For antiskyrmions, the DM vector has an anisotropic interfacial form, given by  $\mathbf{D}_{i,i\pm\hat{\mathbf{x}}} = \pm D\hat{\mathbf{z}} \times \hat{\mathbf{x}}$  for interactions between neighboring sites along  $x$  and  $\mathbf{D}_{i,i\pm\hat{\mathbf{y}}} = \mp D\hat{\mathbf{z}} \times \hat{\mathbf{y}}$  for interactions between neighboring sites along  $y$ , as discussed by Huang *et al.* [60]. The third term is the Zeeman interaction with an applied external magnetic field  $\mathbf{H}$ , where  $\mu = g\mu_B$  is the magnitude of the atomic magnetic moment,  $g = |g_e| = 2.002$  is the electron  $g$ -factor, and  $\mu_B = 9.27 \times 10^{-24}$  J T<sup>-1</sup> is the Bohr magneton. The last term is the sample anisotropy of strength  $K$ . Long-range dipolar interactions act as an anisotropy when considering ultrathin films (see Supplemental Material of Wang *et al.*[61]), therefore shifting the effective anisotropy values.

The time evolution of atomic magnetic moments is obtained using the LLG equation augmented with the spin-orbit torque (SOT) current [62, 63]:

$$\partial_t \mathbf{m}_i = -\gamma \mathbf{m}_i \times \mathbf{H}_i^{\text{eff}} + \alpha \mathbf{m}_i \times \partial_t \mathbf{m}_i + \frac{j\hbar\gamma\theta_{\text{SH}}a^2}{2e\mu} \mathbf{m} \times (\hat{\mathbf{j}} \times \hat{\mathbf{z}}) \times \mathbf{m}. \quad (1)$$

Here  $\gamma = 1.76 \times 10^{11}$  T<sup>-1</sup> s<sup>-1</sup> is the electron gyromagnetic ratio,  $\mathbf{H}_i^{\text{eff}} = -\frac{1}{\mu} \frac{\partial \mathcal{H}}{\partial \mathbf{m}_i}$  is the effective magnetic field including all interactions from the Hamiltonian,  $\alpha$  is the phenomenological damping introduced by Gilbert, and the last term is the torque induced by the spin Hall effect, where  $j$  is the current density,  $\theta_{\text{SH}} = 1$  is the spin Hall angle,  $e$  is the electron charge, and  $\hat{\mathbf{j}}$  is the direction of the current. We fix  $j = 1 \times 10^9$  A m<sup>-2</sup> unless otherwise indicated.

The topological charge  $Q$  is defined as

$$Q = \frac{1}{4\pi} \int \mathbf{m} \cdot \left( \frac{\partial \mathbf{m}}{\partial x} \times \frac{\partial \mathbf{m}}{\partial y} \right) dx dy. \quad (2)$$

In order to guarantee that skyrmions and antiskyrmions have the same topological charge, the applied magnetic field must be modified depending on the texture being simulated. For antiskyrmions and skyrmionium, we use  $\mu \mathbf{H} = 0.5(D^2/J)\hat{\mathbf{z}}$ , and for skyrmions we use  $\mu \mathbf{H} = 0.5(D^2/J)(-\hat{\mathbf{z}})$ .

The material parameters are  $J = 1$  meV,  $D = 0.2J$ ,  $K = 0.01J$ , and  $\alpha = 0.3$ . For each simulation, the system is initialized with the texture of interest. The numerical integration of Eq. 1 is performed using a fourth order Runge-Kutta method.

### 3. Hall angle

We first consider the different textures under an applied dc drive arising from a current  $\mathbf{j}$  where we vary the direction of the drive according to  $\hat{\mathbf{j}} = \cos(\phi)\hat{\mathbf{x}} + \sin(\phi)\hat{\mathbf{y}}$ , where  $\phi$  is the angle between the

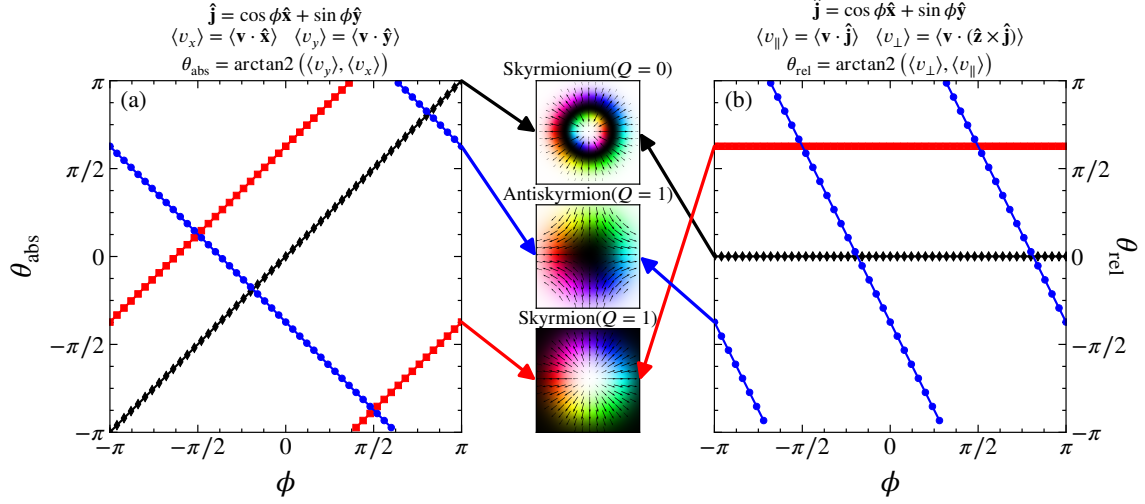


**Figure 1.** (a) Angle  $\theta_{\text{abs}}$  of the absolute motion and (b) angle  $\theta_{\text{rel}}$  of the relative motion vs the applied current angle  $\phi$  for skyrmionium ( $Q = 0$ ) (black diamonds), antiskyrmion ( $Q = 1$ ) (blue circles), and skyrmion ( $Q = 1$ ) (red squares). The center panel shows real-space images of the three textures.

applied external drive and the  $x$  axis. In Fig. 1(a) we show the angle  $\theta_{\text{abs}} = \arctan 2(\langle v_y \rangle, \langle v_x \rangle)$  of the absolute motion of the skyrmionium, antiskyrmion, and skyrmion, while in Fig. 1(b) we plot the angle  $\theta_{\text{rel}} = \arctan 2(\langle v_{\perp} \rangle, \langle v_{\parallel} \rangle)$  of relative motion, where  $v_i$  is the  $i$ -th velocity component of the textures. Note that  $\langle v_{\perp} \rangle$  and  $\langle v_{\parallel} \rangle$  are the texture velocity components perpendicular and parallel to the applied drive, respectively. The center panel shows the real space configuration of the different textures.

In Fig. 1 it is clear that the three textures exhibit different dynamics. The skyrmionium has the simplest behavior: it moves in the same direction as the external drive, so  $\theta_{\text{abs}} = \phi$ , that is, following the rotation of the external drive, and  $\theta_{\text{rel}} = 0$ . This indicates that skyrmionium does not exhibit a Hall effect, in agreement with previous work [53, 56]. The skyrmion shows an offset of the angle in both  $\theta_{\text{abs}}$  and  $\theta_{\text{rel}}$ , indicating the presence of a constant finite Hall angle. On the other hand, the antiskyrmion exhibits a distinct behavior:  $\theta_{\text{abs}}$  has a reversed behavior compared to the skyrmion, while  $\theta_{\text{rel}}$  does not exhibit a constant value. The antiskyrmion has different values of  $\theta_{\text{rel}}$  for different directions of the current, which is in agreement with previous work [44, 46].

#### 4. Interaction with a rigid wall

In this section, to investigate how the different textures interact with a magnetic wall, we drive them toward a line defect of width 4 nm modeled by an anisotropy of  $K_{\text{wall}} = 5J$  that is placed at  $x = 140\text{nm}$  and is infinite along the  $y$  direction. For consistency, we choose a current direction such that all textures move toward the wall at the same angle of  $\theta_{\text{abs}} = \pi/4$  for a fixed current of  $j = 1 \times 10^9 \text{ A m}^{-2}$ . In Fig. 2(a,b,c) we plot  $v_x$  and  $v_y$  versus time for the skyrmionium, skyrmion, and antiskyrmion, and in Fig. 2(d,e,f) we show the corresponding absolute value of the velocity  $v = (v_x^2 + v_y^2)^{1/2}$  versus time. For skyrmionium, the initial free space velocity is  $v_x = v_y = 2.6 \text{ m}$

$\text{s}^{-1}$ . When the skyrmionium interacts with the wall,  $v_x$  drops to zero and there is a slight drop in  $v_y$  to  $v_y = 2.5 \text{ m s}^{-1}$ . The absolute value of the velocity therefore drops from  $v = 3.67 \text{ m s}^{-1}$  to  $v = 2.5 \text{ m s}^{-1}$ , as shown in Fig. 2(d).

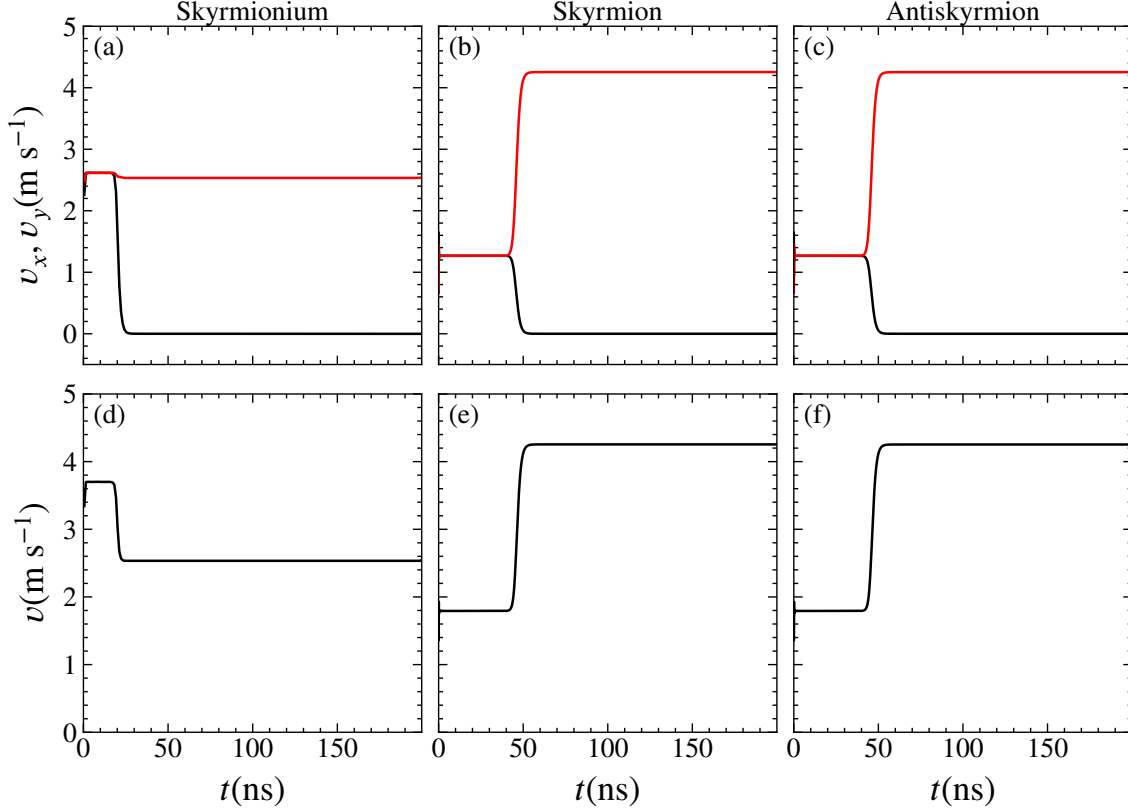
For skyrmions and antiskyrmions, the initial value of  $v_y$  and  $v_x$  is  $1.3 \text{ m s}^{-1}$ , corresponding to half the velocity of skyrmionium, in agreement with previous work indicating that skyrmionium moves faster than skyrmions [53, 56]. When the skyrmion and the antiskyrmion interact with the wall, Fig. 2(e,f) shows that  $v_x$  goes to zero while  $v_y$  shows a strong enhancement to  $v_y = 4.2 \text{ m s}^{-1}$ , and the absolute velocity increases from  $v = 1.80 \text{ m s}^{-1}$ , to  $v = 4.2 \text{ m s}^{-1}$ , indicating a strong velocity boost. A similar velocity boost for skyrmions interacting with line defects was studied previously with both continuum and particle models [29, 30, 31, 32, 33]. The velocity boost arises from the Magnus force, which generates velocity components that are perpendicular to the force experienced by the texture. When the texture moves along a wall, it experiences a velocity component  $v_y$  arising directly from the external drive as well as a Magnus rotation of the  $x$  component of the driving force into the positive  $y$  direction, giving rise to the net boost or speed up in  $v_y$ . The same boost arises for  $Q = \pm 1$ , so the skyrmion and antiskyrmion have the same behavior, while for the skyrmionium, there is no Magnus force and no  $v_y$  boost.

Figure 3(a) shows the dynamics of a skyrmionium interacting with the wall where the coloring indicates the net velocity along each point of the trajectory. The skyrmionium moves at a greater velocity while in free space, and its velocity drops once it comes into contact with the wall. Additionally, the skyrmionium shrinks slightly in size when moving along the barrier due to the pressure exerted by the current. In Fig. 3(b,c), where we show the skyrmion and antiskyrmion, respectively, the textures have the lowest velocity in free space and have enhanced velocity while moving along the barrier.

The skyrmion and antiskyrmion have the same dynamics because they are being driven with different current angles  $\phi$  in order to make both textures interact with the wall at the same absolute angle  $\theta_{\text{abs}}$ . If we choose the same current direction for both textures, the skyrmion and antiskyrmion would move at different angles and approach the wall differently, resulting in a completely different dynamics and impeding the comparison between them.

Next, we consider the case where the texture interacts with a line defect that has a much smaller anisotropy value so that the texture can cross the barrier for large enough drives. We choose the same applied current and wall parameters as described before, but use an anisotropy of  $K = 0.02J$  and vary the current magnitude  $j$ . In Fig. 4(a), we plot the absolute value of the velocity  $\langle v \rangle$  versus  $j$  for the skyrmionium case, where the dashed line indicates the expected behavior in the absence of a barrier. The skyrmionium moves along the wall until  $j = 3.6 \times 10^9 \text{ A m}^{-2}$ . At this drive a jump up appears in the velocity curve, corresponding to the point at which the skyrmionium has sufficient energy provided by the current to cross the barrier. Note that the velocity in the presence of the wall is always lower than the barrier free velocity, and the largest difference between the two velocities occurs at the barrier crossing threshold. For drives above the crossing threshold, the skyrmionium travels with a speed that monotonically approaches the barrier free velocity.

Figure 4(b,c) shows the velocity  $\langle v \rangle$  versus current  $j$  curves for a skyrmion and an antiskyrmion, respectively. Both textures travel along the barrier up to a current of  $j = 2.2 \times 10^9 \text{ A m}^{-2}$  and experience a large velocity boost relative to the barrier free velocity. The velocity difference reaches a maximum at the barrier crossing transition. Once the textures are able to cross the barrier, there is a pronounced drop in the velocity, corresponding to a drop in the Magnus velocity boost. This drop occurs because the Magnus force can no longer convert the barrier force into a perpendicular velocity contribution. For high currents, the velocities approach the barrier free value, and the



**Figure 2.** (a,b,c) Velocities  $v_x$  (black) and  $v_y$  (red) vs time for (a) a skyrmionium with  $\phi = \pi/4$ , (b) a skyrmion with  $\phi = -3\pi/8$ , and (c) an antiskyrmion with  $\phi = -5\pi/8$  driven toward a rigid wall with  $K_{\text{wall}} = 5J$  by a current  $j = 1 \times 10^9 \text{ A m}^{-2}$ . The current angle  $\phi$  is chosen based on the results from Fig. 1 such that  $\theta_{\text{abs}} = \pi/4$  for all of the textures. (d,e,f) The corresponding absolute velocity  $v = (v_x^2 + v_y^2)^{1/2}$  for each texture vs time, showing that the skyrmionium is slowed by the wall but the skyrmion and antiskyrmion experience a velocity boost.

boost effect is completely lost. The results in Figs. 3 and 4 indicate that skyrmionium is strongly affected by pinning or defects, since the threshold current for barrier hopping is large and the velocity of the texture is suppressed by the defects. In contrast, for skyrmions and antiskyrmions, the threshold current for barrier hopping is lower, and the velocity is enhanced by the defects. It is interesting to note that for  $j = 2.2 \times 10^9 \text{ A m}^{-2}$ , the skyrmion and antiskyrmion have even larger velocities than the skyrmionium due to the Magnus velocity boost provided by the Magnus force during interactions with the wall.

## 5. Interaction with a circular defect

In Fig. 5(a,b,c) we illustrate the interaction of a skyrmionium, a skyrmion, and an antiskyrmion, respectively, with a circular defect. We choose the current direction such that the textures all move directly toward the obstacle along the  $x$  direction, giving  $\theta_{\text{abs}} = 0$ . Using  $\hat{\mathbf{j}} = \cos(\phi)\hat{\mathbf{x}} + \sin(\phi)\hat{\mathbf{y}}$ ,

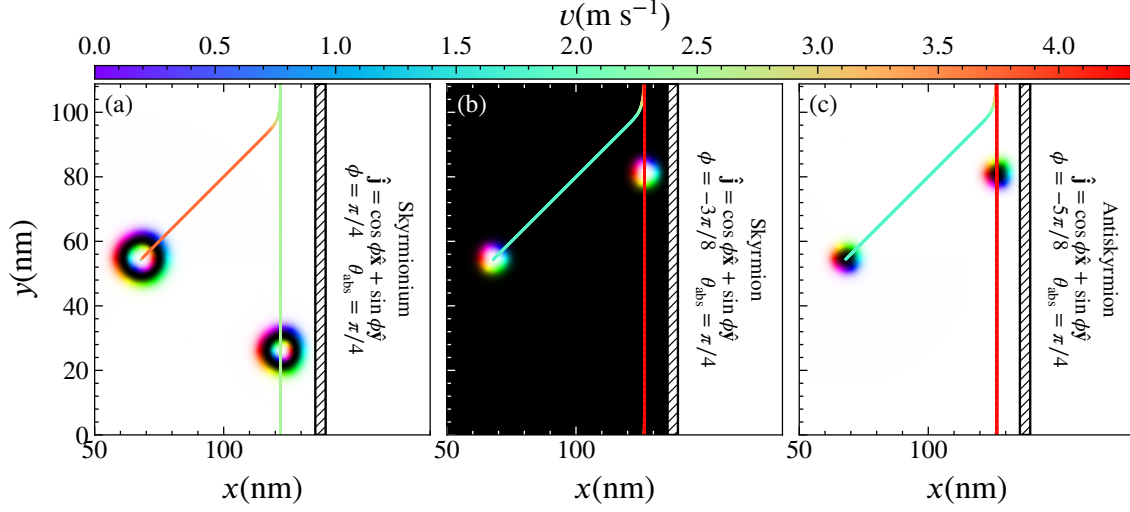


**Figure 3.** Trajectories and selected real space images of (a) a skyrmionium at  $\phi = \pi/4$ , (b) a skyrmion at  $\phi = -3\pi/8$ , and (c) an antiskyrmion at  $\phi = -5\pi/8$  driven towards a rigid wall (hatched region) with  $K_{\text{wall}} = 5J$  by a current  $j = 1 \times 10^9 \text{ A m}^{-2}$ . The wall is represented by the hatched region. The velocity is indicated by a heatmap along the trajectory lines. The current angle is chosen such that  $\theta_{\text{abs}} = \pi/4$  for all textures. Animations showing the motion of the textures are available in the Supplemental material [64].

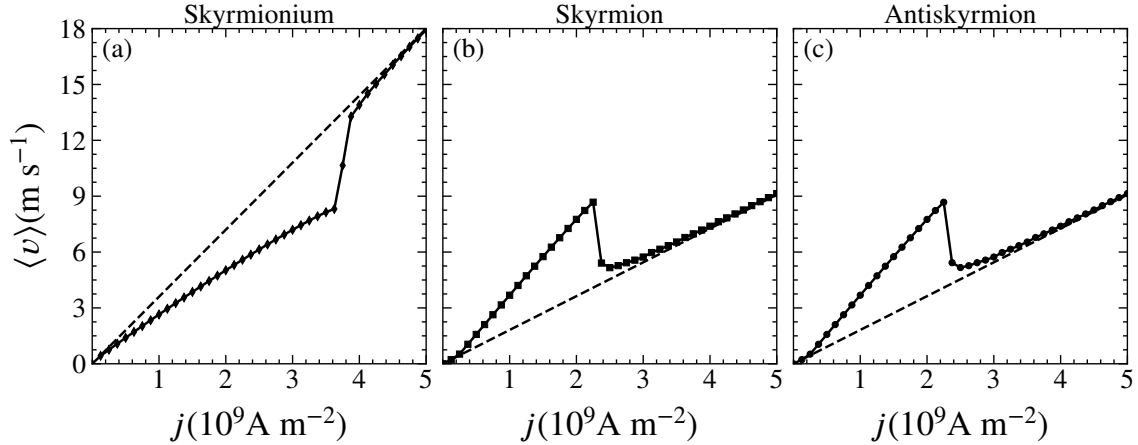


**Figure 4.** Absolute velocity  $\langle v \rangle$  vs current  $j$  for (a) a skyrmionium at  $\phi = \pi/4$ , (b) a skyrmion at  $\phi = -3\pi/8$ , and (c) an antiskyrmion at  $\phi = -5\pi/8$  driven towards a linear defect with  $K = 0.02J$ . The dashed lines are the expected response in the absence of a barrier. The drive directions are chosen such that  $\theta_{\text{abs}} = \pi/4$  for all textures. In (a), the skyrmionium starts hopping over the barrier near  $j = 3.6 \times 10^9 \text{ A m}^{-2}$ , as indicated by an upward jump in  $\langle v \rangle$ . (b,c) The skyrmion and antiskyrmion textures start hopping over the barrier near  $j = 2.2 \times 10^9 \text{ A m}^{-2}$ , as indicated by the jump down in  $\langle v \rangle$ . The skyrmionium velocity is reduced by the barrier, while the barrier boosts the velocity of the skyrmion and the antiskyrmion.

we obtain  $\phi = 0.0$  for the skyrmionium,  $\phi = 5\pi/8$  for the skyrmion, and  $\phi = -3\pi/8$  for the antiskyrmion. For skyrmionium, the net velocity drops nearly to zero for 26 ns before the texture is able to distort enough to escape from the defect and speed up again. The net effect is a slowdown of the skyrmionium when moving towards the defect. For skyrmions and antiskyrmions, the opposite behavior occurs; the textures speed up when interacting with the defect and show a preferred deflection direction.

To quantify the behavior in Fig. 5, in Fig. 6(a,b,c) we plot  $v_x$  and  $v_y$  versus time for the skyrmionium, skyrmion, and antiskyrmion. For skyrmionium, initially  $v_x = 3.8 \text{ m s}^{-1}$ , but  $v_x$  drops nearly to zero for a duration of 26 ns as the texture is temporally pinned behind the defect. The velocity  $v_y$  becomes finite while the skyrmionium distorts its way around the defect. Once the skyrmionium has cleared the defect,  $v_x$  goes back up to  $v_x = 3.8 \text{ m s}^{-1}$  and  $v_y$  returns to zero.

The skyrmions and antiskyrmions easily move or deflect around the obstacle due to the Magnus force, as shown in Fig. 5(b,c). For these textures, Fig. 6(b,c) shows that there is a slight dip in  $v_x$  and a peak in  $v_y$  during the distortion process. The absolute velocity versus time, plotted in Fig. 6(e,f), indicates that there is a boost in the velocity as the textures move past the obstacle. A velocity boost for skyrmions interacting with circular defects has been observed in previous work with both micromagnetic and particle based simulations [27, 65].

It has been argued that skyrmions are generally weakly pinned due to the Magnus force, which allows them to move around defects [66, 15], and the results in Figs. 5 and 6 are in agreement with this picture. The ability of skyrmionium to be pinned depends strongly on both the defect size and the skyrmionium size, but in general, we expect that skyrmionium will be more easily pinned than skyrmions and antiskyrmions. Our results also suggest that with appropriately arranged obstacle patterns, strong skyrmion and antiskyrmion boosting effects could be achieved. Figure 5 also shows that the skyrmions and antiskyrmions have a preferential skew scattering direction when moving around the obstacle, while the skyrmionium does not.

## 6. Interaction between textures

We next consider pairwise interactions between the different textures. In Fig. 7 we plot the energy variation  $\Delta E = E(r) - E(r \rightarrow \infty)$  as a function of the center-to-center distance  $r$  between texture pairs for the skyrmionium, skyrmion, and antiskyrmion systems. The hatched regions indicate values of  $r$  below which the pair of textures merges into a single texture object. To construct these plots, we select two points a distance  $r$  apart to serve as centers for the textures, fix the value of  $\mathbf{m}$  around each center, relax the system, and measure the energy. We then repeat this procedure for a smaller value of  $r$  until we have reached  $r = 0$ . The insets in Fig. 7 show images of the textures at selected values of  $r$ . For skyrmionium, the textures decrease in size as they move closer together, and merge below  $r = 14 \text{ nm}$ . The reduced energy barrier becomes nearly zero above  $r = 40 \text{ nm}$ . For skyrmions and antiskyrmions, the textures do not fuse until  $r = 5 \text{ nm}$ , and  $\Delta E$  reaches zero above  $r = 27 \text{ nm}$ . In general, a skyrmionium is larger than a skyrmion or an antiskyrmion, so a skyrmionium pair has larger repulsive interactions for a given value of  $r$  and merges into a single texture at larger  $r$ . This indicates that for memory device applications involving the use of dense arrays of textures, it would be better to use skyrmion or antiskyrmion textures instead of skyrmionium.



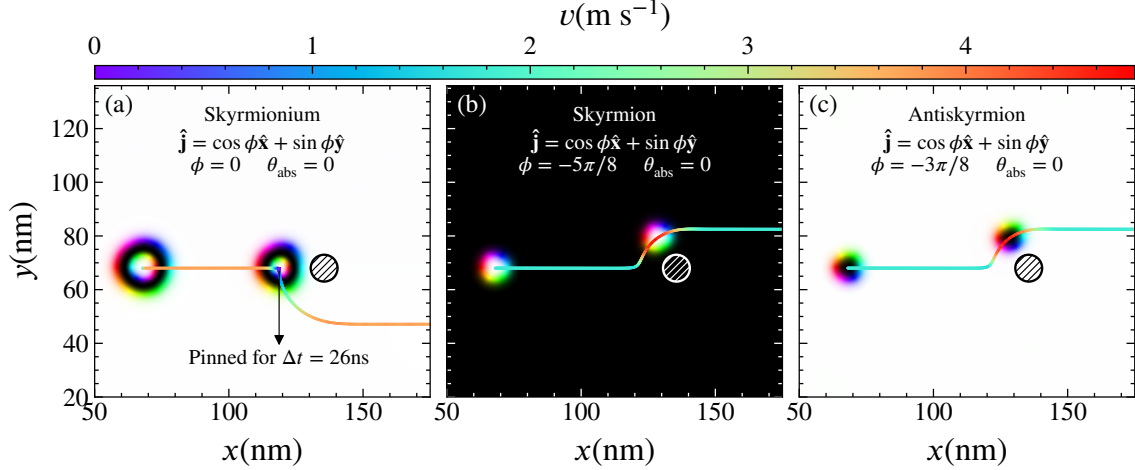


**Figure 5.** Trajectories and selected real space images of (a) a skyrmionium at  $\phi = \pi/4$ , (b) a skyrmion at  $\phi = -3\pi/8$ , and (c) an antiskyrmion at  $\phi = -5\pi/8$  driven toward a circular defect (hatched region) with  $K_{\text{circ}} = 5J$  by a current  $j = 1 \times 10^9 \text{ A m}^{-2}$ . The velocity is indicated by a heatmap along the trajectory lines. The current angle is chosen such that  $\theta_{\text{abs}} = 0$  for all textures. Animations showing the motion of the textures are available in the Supplemental Material [64].

## 7. Dynamics with random disorder

We study the dynamical behavior of the three textures when they are driven over randomly distributed backgrounds of varied anisotropy defects. Each defect has a higher anisotropy than the background anisotropy of the sample. To consistently compare results, we used the same random arrangement of defects for all three textures. We select current angles  $\phi$  such that all of the textures move with  $\theta_{\text{abs}} = 0$ .

In Fig. 8(a,b,c) we plot the absolute velocity  $v$  versus  $j$  for skyrmionium, skyrmion and antiskyrmion systems at different values of anisotropy defect strength  $K$ . As a general behavior, the value of  $j_c$  shifts to higher values for all systems shifts as the anisotropy constant  $K$  increases. The skyrmionium has  $j_c = 3.1 \times 10^9 \text{ A m}^{-2}$  at  $K = 0.18J$ , while for the skyrmion and antiskyrmion systems,  $j_c = 2.5 \times 10^9 \text{ A m}^{-2}$  at  $K = 0.18J$ . That is, the depinning thresholds are higher for the skyrmionium than for the skyrmions and antiskyrmions; however, once the system is in the sliding state, the skyrmionium has the highest velocity.

In Sec. V we showed that skyrmions can easily deflect around defects, suggesting that  $j_c$  should be much lower for skyrmions than for skyrmionium; however, the ability of the skyrmion to deflect around the defects strongly depends on  $j$  because the Magnus force is a strictly dynamical effect [15]. We find that for high currents at  $K > 0.06J$ , the skyrmionium is unstable and transforms into a skyrmion, which is visible as the drop in  $\langle v \rangle$  for  $j > 4 \times 10^9 \text{ A m}^{-2}$ . Previous numerical studies have also shown that skyrmionium is unstable and transforms into a skyrmion at higher drives [55]. In our case, the disorder plays a role in the transformation to the skyrmion state, similar to previous work where a transformation of skyrmionium to a skyrmion upon moving through a constriction was observed [67]. The skyrmion and antiskyrmion remain stable up to much higher currents than the skyrmionium.

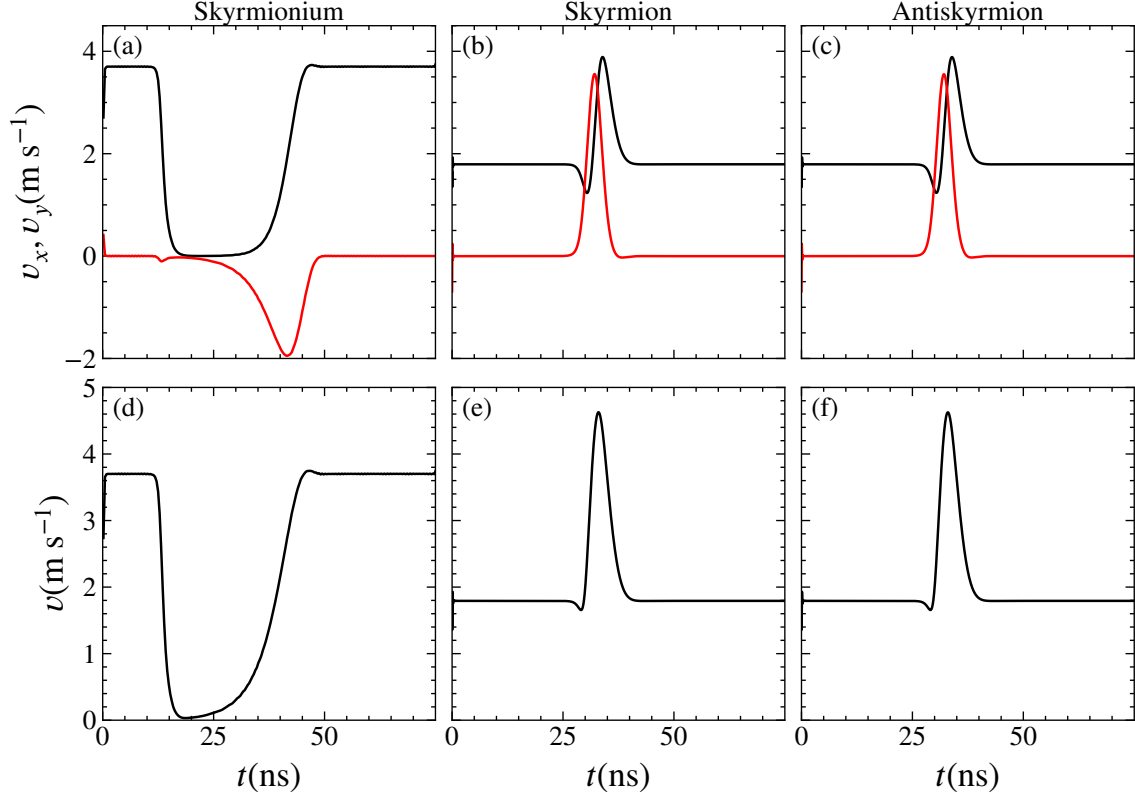


**Figure 6.** (a,b,c) Velocities  $v_x$  (black) and  $v_y$  (red) vs time for (a) a skyrmionium at  $\phi = 0$ , (b) a skyrmion at  $\phi = -5\pi/8$ , and (c) an antiskyrmion at  $\phi = -3\pi/8$  driven toward a circular defect with  $K_{\text{circ}} = 5J$  by a current  $j = 1 \times 10^9 \text{ A m}^{-2}$ . The current angle  $\phi$  is chosen such that  $\theta_{\text{abs}} = 0$  for all textures. (d, e, f) The corresponding absolute velocity  $v$  of each texture vs time.

In Fig. 9(a,b,c), we plot  $\langle v \rangle$  versus  $K/J$  for a skyrmionium, a skyrmion, and an antiskyrmion in the same system from Fig. 8 at  $j = 1 \times 10^9 \text{ A m}^{-2}$ ,  $2 \times 10^9 \text{ A m}^{-2}$ ,  $3 \times 10^9 \text{ A m}^{-2}$ ,  $4 \times 10^9 \text{ A m}^{-2}$ , and  $5 \times 10^9 \text{ A m}^{-2}$ . For a given value of  $j$ , the skyrmionium has a higher velocity than the skyrmion and antiskyrmion; however, for  $j = 5 \times 10^9 \text{ A m}^{-2}$ , there is a drop in the velocity near  $K/J = 0.075$  when the skyrmionium transforms into a skyrmion.

## 8. Diode and Ratchet Effects

To study diode and ratchet effects for the three textures, we introduce the periodic anisotropy pattern shown in Fig. 10, which is described by

$$K(x, y) = \frac{0.015J}{136} \text{mod} \left( x, \frac{136}{3} \right) + 0.01J. \quad (3)$$

This pattern was used previously in work on ratchet effects in particle based skyrmion systems [68, 15]. There have also been a variety of studies on diode and ratchet effects for skyrmions in

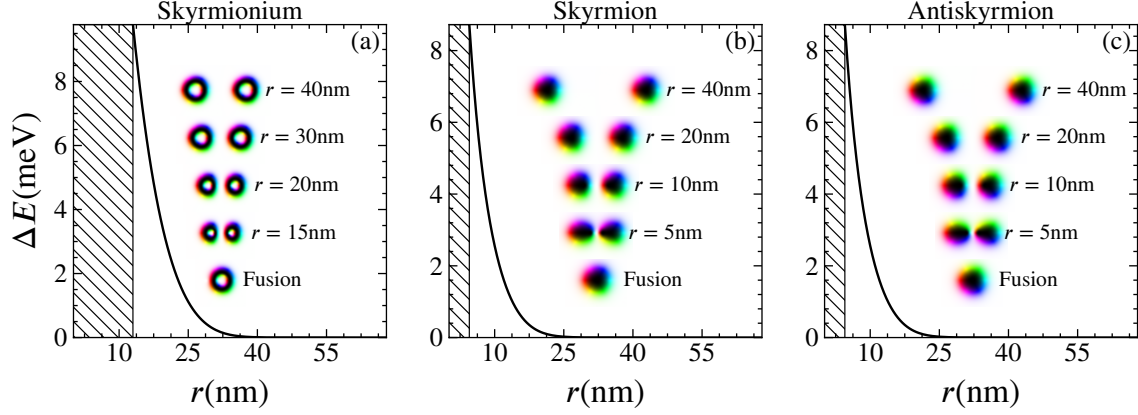


**Figure 7.** Energy variation  $\Delta E = E(r) - E(r \rightarrow \infty)$  as a function of the center-to-center distance between textures for (a) skyrmionium (b) skyrmion, (c) antiskyrmion. The hatched regions indicate where the textures have fused. The images show the texture configurations at different  $r$ .

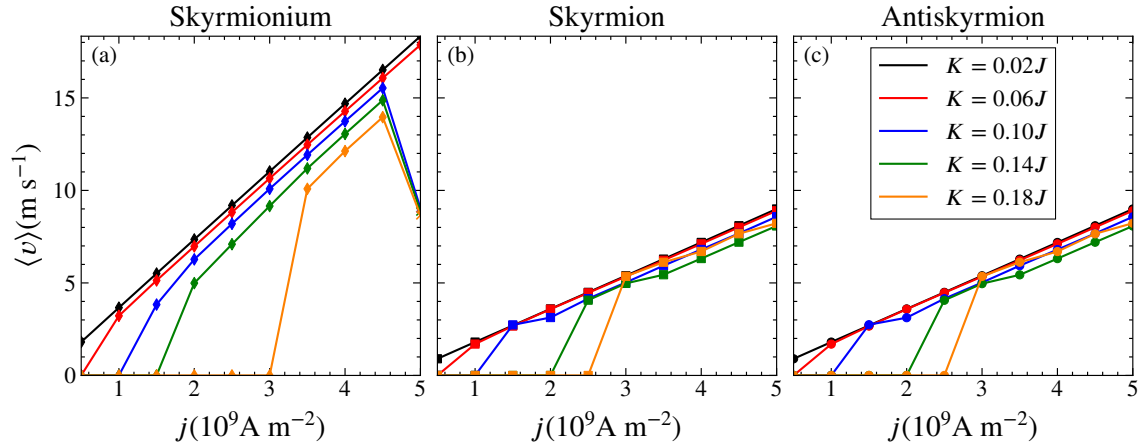


**Figure 8.** Average velocity  $\langle v \rangle$  vs current density  $j$  for different values of anisotropy defect strength  $K = 0.02J$  (black),  $0.06J$  (red),  $0.10J$  (blue),  $0.14J$  (green), and  $0.18J$  (orange) for (a) a skyrmionium with  $\phi = 0$ , (b) a skyrmion with  $\phi = -5\pi/8$ , and (c) an antiskyrmion with  $\phi = -3\pi/8$ . For these choices of  $\phi$ , all of the textures move with  $\theta_{\text{abs}} = 0$ .

systems with various types of asymmetric substrates or barriers [39, 34, 40, 35, 69, 37, 36, 38]. Some of these studies showed that the Magnus force can be used to generate or enhance the ratchet effect. There has also been work showing that diode effects could occur for skyrmionium interacting with a magnetic anisotropy [34].

In Fig. 11(a,b,c) we plot the absolute value of the velocity  $|\langle v_x \rangle|$  versus  $|j|$  for a skyrmionium, a skyrmion, and an antiskyrmion. The skyrmionium depins in the easy direction ( $j > 0$ ) at  $|j| = 0.5 \times 10^9 \text{ A m}^{-2}$ , while it depins in the hard direction ( $j < 0$ ) at  $|j| = 0.75 \times 10^9 \text{ A m}^{-2}$ , indicating the presence of a diode effect. For the skyrmion and the antiskyrmion, sliding begins

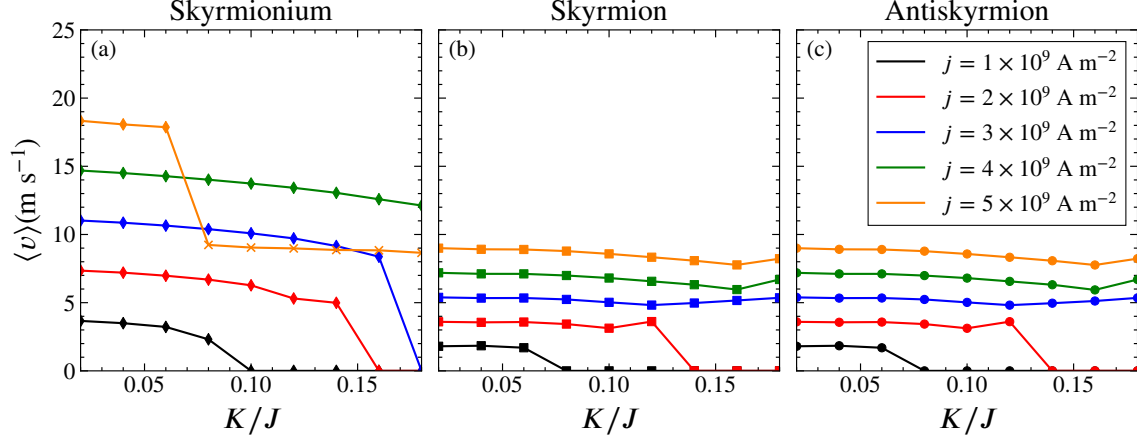


**Figure 9.** Average velocity  $\langle v \rangle$  vs scaled anisotropy defect strength  $K/J$  at different values of current density  $j = 1 \times 10^9$  A m<sup>-2</sup> (black),  $2 \times 10^9$  A m<sup>-2</sup> (red),  $3 \times 10^9$  A m<sup>-2</sup> (blue),  $4 \times 10^9$  A m<sup>-2</sup> (green), and  $5 \times 10^9$  A m<sup>-2</sup> (yellow) for (a) a skyrmionium at  $\phi = 0$ , (b) a skyrmion at  $\phi = -5\pi/8$ , and (c) an antiskyrmion at  $\phi = -3\pi/8$ . The different choices of  $\phi$  ensure that  $\theta_{\text{abs}} = 0$  for all textures.

at  $|j| = 0.25 \times 10^9$  A m<sup>-2</sup> in the easy direction and  $|j| = 0.6 \times 10^9$  A m<sup>-2</sup> in the hard direction. All of the textures show a diode effect; however, the skyrmionium is more strongly pinned in both driving directions.

The plots of  $\langle v_y \rangle$  versus  $|j|$  in Fig. 11(d,e,f) show that  $\langle v_y \rangle$  is zero for the skyrmionium but is finite for the skyrmion and antiskyrmion. When  $\langle v_x \rangle = 0.0$ , the skyrmionium is completely pinned, but the skyrmion and antiskyrmion can move along the substrate troughs in the  $y$ -direction in a manner similar to that found for the interaction of the textures with line defects in Sec. IV. The  $y$ -component velocity of the skyrmion and antiskyrmion reaches a maximum near the current at which the textures become able to hop over the barrier in the  $x$  direction, and above this transition  $v_y$  decreases with increasing drive. This result indicates that there is a diode effect for motion in both the  $x$  and  $y$  directions for skyrmions and antiskyrmions.

Figure 11(g,h,i) shows the absolute velocity  $\langle v \rangle$  versus  $|j|$  for the three textures. For the skyrmionium,  $\langle v \rangle = |\langle v_x \rangle|$ , but this is not true for the skyrmion and antiskyrmion. From the absolute velocity we find that there is no minimum threshold current for motion of the skyrmion or antiskyrmion, and that both textures can slide along the barrier troughs for arbitrarily low values of  $j$ . Interestingly, the absolute velocity is higher for driving in the hard direction than for driving in the easy direction, opposite to the behavior found for skyrmionium. The increase of  $\langle v \rangle$  for hard direction driving in the skyrmion and antiskyrmion systems is the result of the Magnus velocity boost, as described in Sec. IV for interaction with a line defect.

We next consider ratchet effects by combining the potential of Eq. (4) with ac driving of the form  $\mathbf{j}_{\text{ac}} = j \sin(2\pi ft) \hat{\mathbf{j}}_{\text{ac}}$ . Here  $f = 10$  MHz and  $j = 9 \times 10^8$  A m<sup>-2</sup>. The ac driving direction  $\hat{\mathbf{j}}_{\text{ac}} = \cos \phi \hat{\mathbf{x}} + \sin \phi \hat{\mathbf{y}}$  is different for each texture to ensure that all textures move with  $\theta_{\text{abs}} = 0$ . This is achieved by setting  $\phi = 0$  for the skyrmionium,  $\phi = -5\pi/8$  for the skyrmion, and  $\phi = -3\pi/8$  for the antiskyrmion. In Fig. 12(a,b,c), we illustrate the trajectories of a skyrmionium, a skyrmion, and an antiskyrmion under the ac driving. The skyrmionium has no  $y$  direction motion but moves

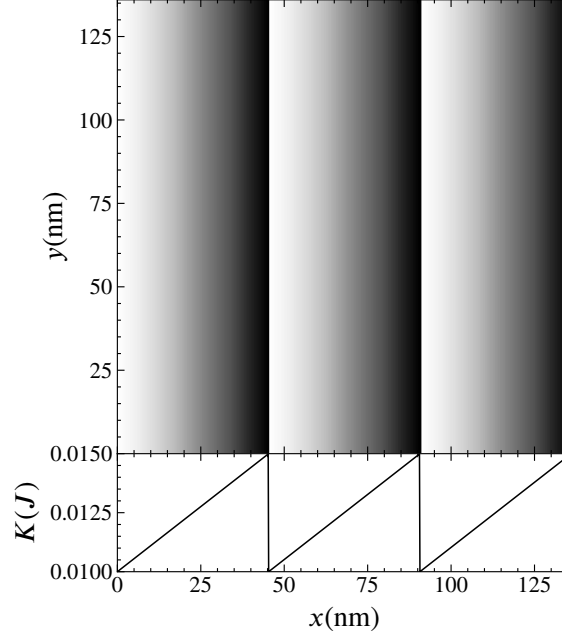


**Figure 10.** Top: Height field illustration of the periodic asymmetric potential given by Eq. 3 with a period of 45 nm. Bottom: The corresponding  $K$  in units of  $J$  vs  $x$ .

back and forth along the  $x$  direction to give a net translation in  $x$ , which is along the same direction as the applied current  $\hat{\mathbf{j}}_{\text{ac}}$  since the skyrmionium Hall angle is zero. This motion is the same as that found for an overdamped particle, such as a superconducting vortex, on a substrate of this type. The skyrmion and antiskyrmion textures follow much more complicated two-dimensional orbits with motion in both the  $x$  and  $y$  directions, resulting in a net dc ratchet transport along both  $x$  and  $y$ . These more complicated orbits result from the finite Magnus force. Previous work on skyrmion ratchets also found complex two-dimensional orbits where the Magnus force plays a strong role in the motion [15].

To measure the efficiency of the ratchet effect, in Fig. 13(a,b,c) we plot the net  $x$  direction displacement  $\Delta x$  versus time along with an arrow indicating the direction of  $\hat{\mathbf{j}}_{\text{ac}}$  for the three textures from Fig. 12. Here  $\Delta x$  increases as a function of time with the same rate for all textures, indicating the appearance of a ratchet effect in the  $+x$  direction. Figure 13(d,e,f) shows the corresponding net  $y$  displacement  $\Delta y$  versus time. For the skyrmionium,  $\Delta y = 0.0$ , indicating that the motion is confined to one dimension and occurs only along the  $x$  direction, as indicated in Fig. 12(a). In contrast, the skyrmion and antiskyrmion show a pronounced net motion in the  $-y$  direction, as also found in Fig. 12(b,c). The plots of  $\Delta r = (\Delta x^2 + \Delta y^2)^{1/2}$  versus time in Fig. 13(g,h,i) show that the skyrmionium has a net translation of nearly  $1 \mu\text{m}$  in  $2 \mu\text{s}$ , while the skyrmion and antiskyrmion move a net distance of over  $2 \mu\text{m}$  in the same amount of time, indicating that the ratchet efficiency is twice as large for the skyrmion and antiskyrmion as for the skyrmionium. The Magnus boost effect found for the skyrmions and antiskyrmions produces a much larger ratchet effect for a given substrate strength compared to skyrmionium. We note that if we set  $\hat{\mathbf{j}}_{\text{ac}}$  to the

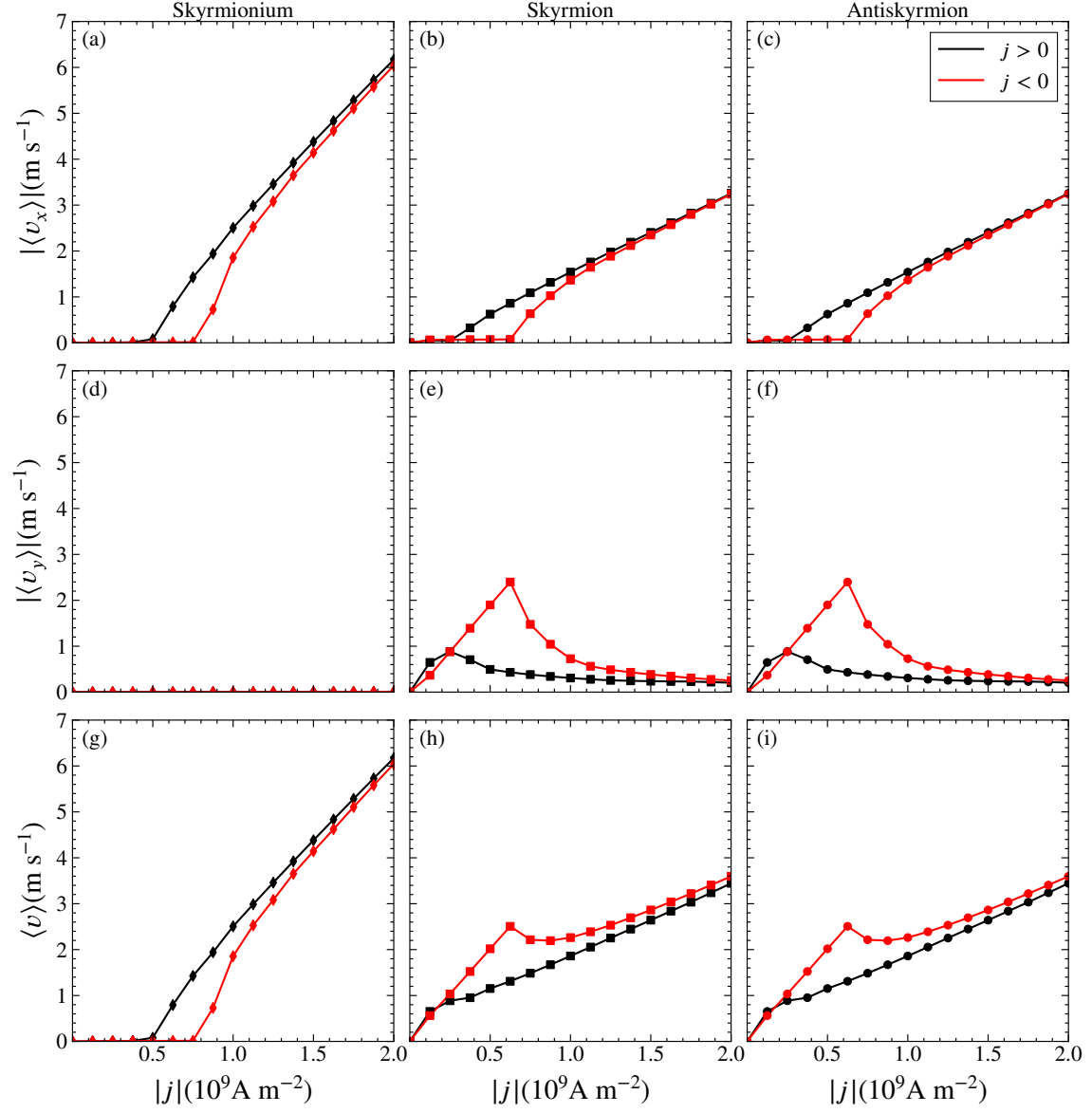


**Figure 11.** (a,b,c) Average velocity  $\langle v_x \rangle$  versus current density  $|j|$  for  $j > 0$  (black) and  $j < 0$  (red) showing the diode effect for the system in Fig. 10. (d,e,f) The corresponding  $\langle v_y \rangle$  vs  $|j|$ . (g,h,i) The corresponding  $\langle v \rangle$  vs  $|j|$ . The textures are (a,d,g) a skyrmionium, (b,e,h) a skyrmion, and (c,f,i) an antiskyrmion.

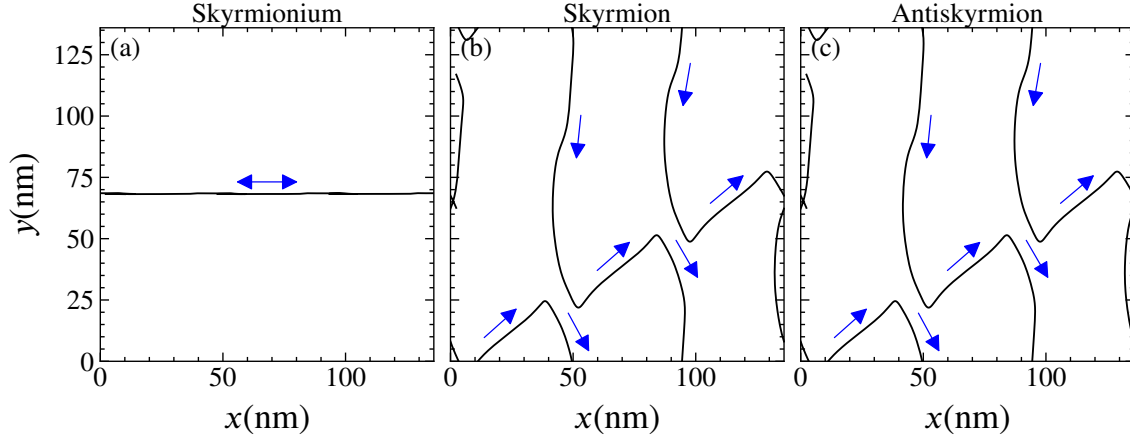


**Figure 12.** The trajectories of the textures in the ratcheting state under ac driving with  $j = 9 \times 10^8 \text{ A m}^{-2}$  over the asymmetric potential illustrated in Fig. 10. The ac driving direction  $\phi$  is chosen such that all of the textures move with  $\theta_{\text{abs}} = 0$ . (a) A skyrmionium at  $\phi = 0$  shows only one dimensional motion along  $x$ . (b) A skyrmion and (c) an antiskyrmion follow a complex orbit in  $x$  and  $y$  that produces ratchet transport in both directions.

same value for all three textures, we would obtain different results for each texture, with the ratchet effect disappearing entirely in some cases.

## 9. Discussion

Our results show that the skyrmionium, skyrmion, and antiskyrmion textures each have advantages and disadvantages for possible future applications. An important advantage of skyrmionium is that it moves without a Hall angle, so it can travel down a narrow channel without being annihilated by the channel edge. Additionally, in the absence of a defect, the skyrmionium moves twice as fast as a skyrmion or an antiskyrmion, which can be useful for fast operations. Skyrmionium has the disadvantage that it is more strongly pinned by defects, so if a fabricated geometry contained disorder, larger currents would be required to initiate the motion of the skyrmionium. Another disadvantage is that the skyrmionium destabilizes and breaks up into a skyrmion at higher currents, and the current at which this breakup occurs shifts to lower values when disorder is present. Skyrmions and antiskyrmions have the advantage of remaining stable up to much higher drives, well beyond the drives we considered in this work. Skyrmionium is not as strongly pinned or slowed down by circular defects compared to skyrmions and antiskyrmions. A line defect can produce a substantial boosting of the velocity of skyrmions and antiskyrmions due to the Magnus force, but slows the motion of a skyrmionium; as a result, skyrmions and antiskyrmions can, in some cases, move faster than skyrmionium along a line defect. Skyrmions and antiskyrmions also exhibit more pronounced ratchet effects than skyrmionium. Certain memory applications require a high density of particles, and since skyrmions and antiskyrmions are smaller than skyrmionium, they can be assembled into higher density structures before fusing or annihilating compared to skyrmionium.

Throughout this work, we chose drive angles  $\phi$  such that  $\theta_{\text{abs}} = 0$  for all of the textures, and as a result, the skyrmion and antiskyrmion generally showed identical behavior. For skyrmions, the

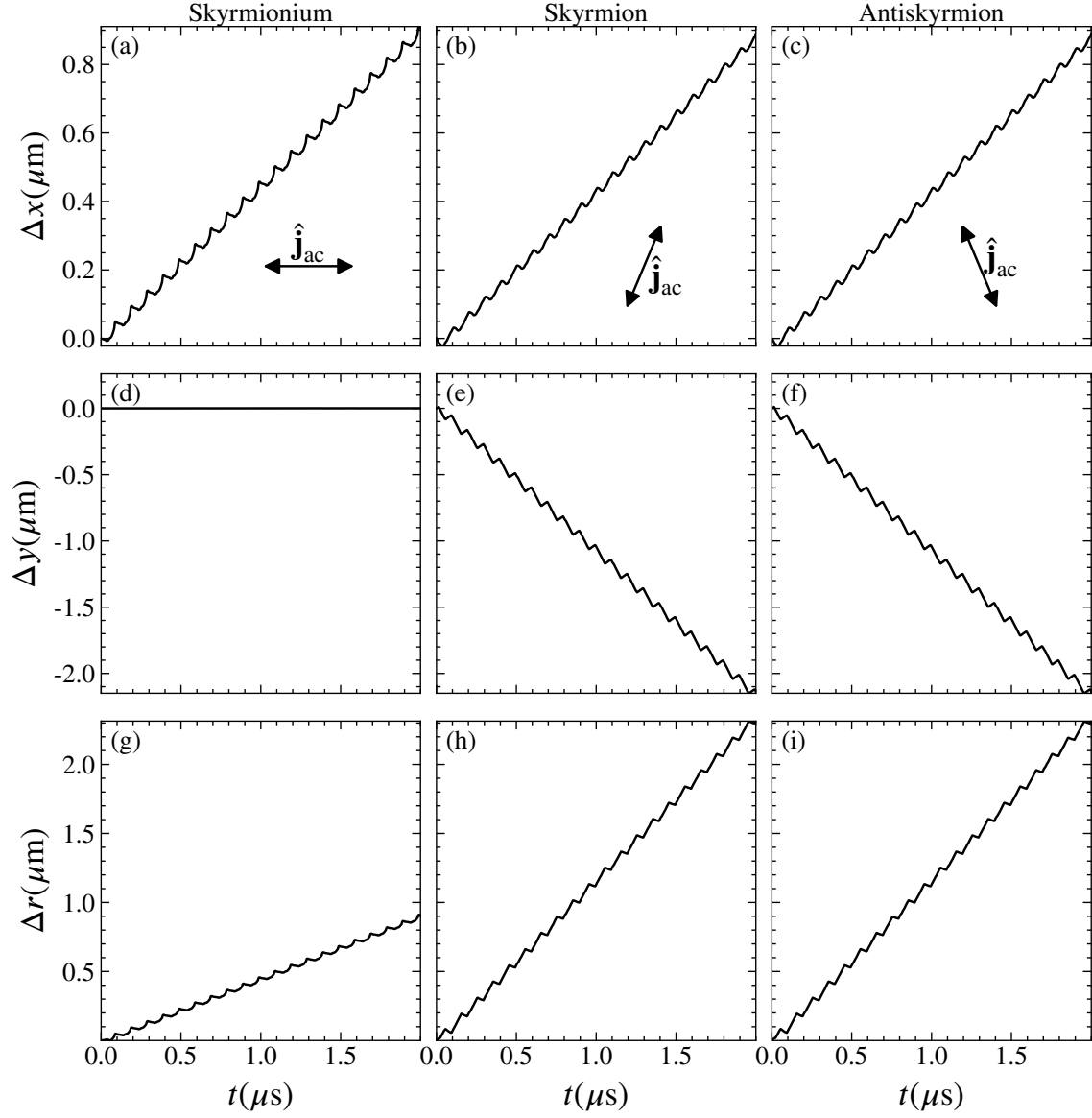


**Figure 13.** (a,b,c) Displacement along the  $x$  direction  $\Delta x$  vs time  $t$  for  $j = 9 \times 10^8 \text{ A m}^{-2}$ . The arrows indicate the direction of ac driving. (d,e,f) The corresponding  $\Delta y$  vs  $t$ . (g,h,i) The corresponding  $\Delta r$  vs  $t$ . (a,d,g) A skyrmionium at  $\phi = 0$ . (b,e,h) A skyrmion at  $\phi = -5\pi/8$ . (c,f,i) An antiskyrmion at  $\phi = -3\pi/8$ . The values of  $\phi$  are chosen such that all of the textures move with  $\theta_{\text{abs}} = 0$ .



Hall angle is constant regardless of the choice of drive angle  $\phi$ ; however, for antiskyrmions, the Hall angle varies as  $\phi$  changes. This could mean that for values of  $\phi$  different from those studied here, the Hall angle could be lower for the antiskyrmions than for the skyrmions; however, for applications in which it is necessary to transport textures along both the  $x$  and  $y$  directions, such as braiding operations, skyrmions are a better choice than antiskyrmions [70], since the varying Hall angle would require a much more complex driving protocol to be used in order to translate the antiskyrmions compared to the skyrmions. One texture we did not consider is the antiferromagnetic skyrmion [40], which has similar dynamics to skyrmionium, but could be more stable at higher drives.

Some other interesting questions we did not address in this work include the effects of thermal stability and diffusion. It is possible that skyrmionium would have lower diffusion or smaller creep than skyrmions and antiskyrmions since it is a larger texture, and it is also possible that thermal effects could cause skyrmionium to break up into a skyrmion. We also did not consider the effect of applying circular driving rather than linear ac driving.

## 10. Summary

We have compared the dynamics of skyrmionium, skyrmion, and antiskyrmion textures interacting with line defects, circular defects, random disorder landscapes, and asymmetric potentials. For dc driving, the skyrmionium moves in the same direction as the current so there is no Hall angle. The skyrmion moves at a fixed Hall angle, and the Hall angle of the antiskyrmion depends on the direction of the current. In this work, we select our driving direction  $\phi$  such that the absolute motion angle  $\theta_{\text{abs}} = 0$  for all of the textures in order to permit us to perform a consistent comparison of the different dynamics.

For motion along a line defect, the skyrmionium slows down compared to motion in free space, but the skyrmion and antiskyrmion speed up due to a Magnus induced boost effect. For penetrable walls, the velocity-force curve for the skyrmionium always falls below the barrier free curve, and there is a jump up in the velocity when the drive increases above the barrier hopping threshold. For skyrmions and antiskyrmions, the velocity is always boosted to a value greater than that for motion in the absence of a barrier, and there is a local maximum in the velocity at the barrier hopping threshold drive. The hopping threshold is much larger for skyrmionium than for skyrmions and antiskyrmions. When interacting with a circular defect, a skyrmionium slows down and becomes temporarily pinned, while the skyrmion and antiskyrmion textures deflect easily around the defect and experience a velocity boost. Skyrmionium has the highest depinning threshold for driving over random disorder, but in the sliding state the skyrmionium velocity is twice as large as that of the skyrmion and antiskyrmion textures. At high drives, the skyrmionium breaks up into a skyrmion, limiting the range of currents that can be applied to the skyrmionium.

When a quasi-one-dimensional asymmetric substrate is introduced, the skyrmionium shows a diode effect in which the depinning threshold is higher for driving in one direction than the other. The skyrmions and antiskyrmions do not have a finite depinning threshold since they can slide along the barrier troughs even for driving applied perpendicular to the barrier troughs, and there is a peak in the net skyrmion or antiskyrmion velocity at the threshold current for crossing the substrate barriers. When ac driving is applied perpendicular to the barrier troughs, skyrmionium can exhibit a one-dimensional ratchet effect along the driving direction, while the skyrmion and antiskyrmion ratchet along both the  $x$  and  $y$  direction and follow complex two-dimensional orbits due to the Magnus force. The net ratchet efficiency can be twice as large for skyrmion and antiskyrmion textures than for skyrmionium due to the Magnus force.

In general, we find that the dynamics of skyrmions and antiskyrmions are very similar. We discuss the advantages and disadvantages of each texture for applications. Skyrmionium has a zero Hall angle and can move faster in free space, but it is more easily pinned by defects and is limited to use only for lower currents since it destabilizes at higher currents. Skyrmions and antiskyrmions have a finite Hall angle and move more slowly than skyrmionium in free space, but in the presence of disorder, the Magnus effect can strongly boost their velocity even above that of skyrmionium, and they are much more stable than skyrmionium at high drives.

## Acknowledgments

This work was supported by the US Department of Energy through the Los Alamos National Laboratory. Los Alamos National Laboratory is operated by Triad National Security, LLC, for the National Nuclear Security Administration of the U. S. Department of Energy (Contract No. 892333218NCA000001). J.C.B.S and N.P.V. acknowledge funding from Fundação de Amparo à Pesquisa do Estado de São Paulo - FAPESP (Grants 2023/17545-1 and 2024/13248-5, respectively). We would like to thank FAPESP for providing the computational resources used in this work (Grant: 2024/02941-1).

## References

- [1] S. Mühlbauer, B. Binz, F. Jonietz, C. Pfleiderer, A. Rosch, A. Neubauer, R. Georgii, and P. Böni. Skyrmion lattice in a chiral magnet. *Science*, 323(5916):915–919, 2009.
- [2] X. Z. Yu, Y. Onose, N. Kanazawa, J. H. Park, J. H. Han, Y. Matsui, N. Nagaosa, and Y. Tokura. Real-space observation of a two-dimensional skyrmion crystal. *Nature (London)*, 465(7300):901–904, 2010.
- [3] N. Nagaosa and Y. Tokura. Topological properties and dynamics of magnetic skyrmions. *Nature Nanotechnol.*, 8(12):899–911, 2013.
- [4] F. Jonietz, S. Mühlbauer, C. Pfleiderer, A. Neubauer, W. Münzer, A. Bauer, T. Adams, R. Georgii, P. Böni, R. A. Duine, K. Everschor, M. Garst, and A. Rosch. Spin transfer torques in MnSi at ultralow current densities. *Science*, 330(6011):1648–1651, 2010.
- [5] X. Z. Yu, N. Kanazawa, W. Z. Zhang, T. Nagai, T. Hara, K. Kimoto, Y. Matsui, Y. Onose, and Y. Tokura. Skyrmion flow near room temperature in an ultralow current density. *Nature Commun.*, 3:988, 2012.
- [6] U. Ritzmann, S. von Malottki, J.-V. Kim, S. Heinze, J. Sinova, and B. Dupé. Trochoidal motion and pair generation in skyrmion and antiskyrmion dynamics under spin-orbit torques. *Nature Electron.*, 1(8):451–457, 2018.
- [7] R. Nepal, U. Güngördü, and A. A. Kovalev. Magnetic skyrmion bubble motion driven by surface acoustic waves. *Appl. Phys. Lett.*, 112(11):112404, 2018.
- [8] Z. Wang, M. Guo, H.-A. Zhou, L. Zhao, T. Xu, R. Tomasello, H. Bai, Y. Dong, S.-G. Je, W. Chao, H.-S. Han, S. Lee, K.-S. Lee, Y. Yao, W. Han, C. Song, H. Wu, Carpentieri M., G. Finocchio, M.-Y. Im, S.-Z. Lin, and W. Jiang. Thermal generation, manipulation and thermoelectric detection of skyrmions. *Nature Electron.*, 3:672, 2020.
- [9] S.-Z. Lin, C. Reichhardt, C. D. Batista, and A. Saxena. Particle model for skyrmions in metallic chiral magnets: Dynamics, pinning, and creep. *Phys. Rev. B*, 87:214419, 2013.
- [10] C. Hanneken, A. Kubetzka, K. von Bergmann, and R. Wiesendanger. Pinning and movement of individual nanoscale magnetic skyrmions via defects. *New J. Phys.*, 18:055009, 2016.
- [11] I. L. Fernandes, J. Bouaziz, S. Blügel, and S. Lounis. Universality of defect-skyrmion interaction profiles. *Nature Commun.*, 9:4395, 2018.
- [12] C. Navau, N. Del-Valle, and A. Sanchez. Interaction of isolated skyrmions with point and linear defects. *J. Mag. Mag. Mater.*, 465:709–715, 2018.
- [13] D. Toscano, S. A. Leonel, P. Z. Coura, and F. Sato. Building traps for skyrmions by the incorporation of magnetic defects into nanomagnets: Pinning and scattering traps by magnetic properties engineering. *J. Mag. Mag. Mater.*, 480:171–185, 2019.
- [14] I. G. Arjana, I. L. Fernandes, J. Chico, and S. Lounis. Sub-nanoscale atom-by-atom crafting of skyrmion-defect interaction profiles. *Sci. Rep.*, 10:14655, 2020.

- [15] C. Reichhardt, C. J. O. Reichhardt, and M. Milosevic. Statics and dynamics of skyrmions interacting with disorder and nanostructures. *Rev. Mod. Phys.*, 94:035005, 2022.
- [16] N. P. Vizari, C. Reichhardt, C. J. O. Reichhardt, and P. A. Venegas. Skyrmion dynamics and topological sorting on periodic obstacle arrays. *New J. Phys.*, 22:053025, 2020.
- [17] R. Juge, K. Bairagi, K. G. Rana, J. Vogel, M. Sall, D. Mailly, V. T. Pham, Q. Zhang, N. Sisodia, M. Foerster, L. Aballe, M. Belmuguenai, Y. Roussigné, S. Auffret, L. D. Buda-Prejbeanu, G. Gaudin, D. Ravelosona, and O. Boulle. Helium ions put magnetic skyrmions on the track. *Nano Lett.*, 21:2989–2996, 2021.
- [18] A. Fert, V. Cros, and J. Sampaio. Skyrmions on the track. *Nature Nanotechnol.*, 8(3):152–156, 2013.
- [19] G. Finocchio, F. Büttner, R. Tomasello, M. Carpentieri, and M. Kläui. Magnetic skyrmions: from fundamental to applications. *J. Phys. D: Appl. Phys.*, 49(42):423001, 2016.
- [20] J. Grollier, D. Querlioz, K. Y. Camsari, K. Everschor-Sitte, S. Fukami, and M. D. Stiles. Neuromorphic spintronics. *Nature Electron.*, 3(7):360–370, 2020.
- [21] K. Litzius, I. Lemesh, B. Krüger, P. Bassirian, L. Caretta, K. Richter, F. Büttner, K. Sato, O. A. Tretiakov, J. Förster, R. M. Reeve, M. Weigand, I. Bykova, H. Stoll, G. Schütz, G. S. D. Beach, and M. Kläui. Skyrmion Hall effect revealed by direct time-resolved X-ray microscopy. *Nature Phys.*, 13(2):170–175, 2017.
- [22] W. Jiang, X. Zhang, G. Yu, W. Zhang, X. Wang, M. B. Jungfleisch, J. E. Pearson, X. Cheng, O. Heinonen, K. L. Wang, Y. Zhou, A. Hoffmann, and S. G. E. te Velthuis. Direct observation of the skyrmion Hall effect. *Nature Phys.*, 13(2):162–169, 2017.
- [23] C. Reichhardt and C. J. O. Reichhardt. Plastic flow and the skyrmion Hall effect. *Nature Commun.*, 11:738, 2020.
- [24] N. Del-Valle, J. Castell-Queralt, L. González-Gómez, and C. Navau. Defect modeling in skyrmionic ferromagnetic systems. *APL Mater.*, 10:101702, 2022.
- [25] Xichao Zhang, Jing Xia, Oleg A. Tretiakov, Motohiko Ezawa, Guoping Zhao, Yan Zhou, Xiaoxi Liu, and Masahito Mochizuki. Laminar and transiently disordered dynamics of magnetic-skyrmion pipe flow. *Physical Review B*, 108:144428, 2023.
- [26] R. C. Silva, R. L. Silva, J. C. Moreira, W. A. Moura-Melo, and A. R. Pereira. Channeling skyrmions: Suppressing the skyrmion hall effect in ferrimagnetic nanostripes. *Journal of Applied Physics*, 135:183902, 2024.
- [27] J. Müller and A. Rosch. Capturing of a magnetic skyrmion with a hole. *Phys. Rev. B*, 91:054410, 2015.
- [28] I. L. Fernandes, J. Chico, and S. Lounis. Impurity-dependent gyrotropic motion, deflection and pinning of current-driven ultrasmall skyrmions in PdFe/Ir(111) surface. *J. Phys.: Condens. Matter*, 32:425802, 2020.
- [29] J. Iwasaki, W. Koshibae, and N. Nagaosa. Colossal spin transfer torque effect on skyrmion along the edge. *Nano Lett.*, 14:4432–4437, 2014.
- [30] C. Reichhardt and C. J. Olson Reichhardt. Magnus-induced dynamics of driven skyrmions on a quasi-one-dimensional periodic substrate. *Phys. Rev. B*, 94:094413, 2016.
- [31] C. Navau, N. Del-Valle, and A. Sanchez. Analytical trajectories of skyrmions in confined geometries: Skyrmionic racetracks and nano-oscillators. *Phys. Rev. B*, 94:184104, 2016.
- [32] X. Chen, W. Kang, D. Zhu, X. Zhang, N. Lei, Y. Zhang, Y. Zhou, and W. Zhao. Skyrmion dynamics in width-varying nanotracks and implications for skyrmionic applications. *Appl. Phys. Lett.*, 111:202406, 2017.
- [33] J. Castell-Queralt, L. Gonzalez-Gomez, N. Del-Valle, A. Sanchez, and C. Navau. Accelerating, guiding, and compressing skyrmions by defect rails. *Nanoscale*, 11(26):12589–12594, 2019.
- [34] J. Wang, J. Xia, X. Zhang, X. Zheng, G. Li, L. Chen, Y. Zhou, J. Wu, H. Yin, R. Chantrell, and Y. Xu. Magnetic skyrmionium diode with a magnetic anisotropy voltage gating. *Appl. Phys. Lett.*, 117(20):202401, 2020.
- [35] D.-H. Jung, H.-S. Han, N. Kim, G. Kim, S. Jeong, S. Lee, M. Kang, M.-Y. Im, and K.-S. Lee. Magnetic skyrmion diode: Unidirectional skyrmion motion via symmetry breaking of potential energy barriers. *Phys. Rev. B*, 104:L060408, 2021.
- [36] Y. Shu, Q. Li, J. Xia, P. Lai, Z. Hou, Y. Zhao, D. Zhang, Y. Zhou, X. Liu, and G. Zhao. Realization of the skyrmionic logic gates and diodes in the same racetrack with enhanced and modified edges. *Appl. Phys. Lett.*, 121:042402, 2022.
- [37] Y. Feng, X. Zhang, G. Zhao, and G. Xiang. A skyrmion diode based on skyrmion Hall effect. *IEEE Trans. Electron Devices*, 69:1293, 2022.
- [38] J. C. Bellizotti Souza, N. P. Vizari, C. J. O. Reichhardt, C. Reichhardt, and P. A. Venegas. Magnus induced diode effect for skyrmions in channels with periodic potentials. *Journal of Physics: Condensed Matter*, 35:015804, 2022.
- [39] R. Yamaguchi, K. Yamada, and Y. Nakatani. Control of current-induced skyrmion motion in ratchet-type skyrmion-based racetrack memory with a loop structure. *Japan. J. Appl. Phys.*, 60:010904, 2020.
- [40] B. Göbel and I. Mertig. Skyrmion ratchet propagation: utilizing the skyrmion Hall effect in AC racetrack storage devices. *Sci. Rep.*, 11:3020, 2021.

- [41] J. C. Bellizotti Souza, N. P. Vizariim, C. J. O. Reichhardt, C. Reichhardt, and P. A. Venegas. Skyrmion ratchet in funnel geometries. *Phys. Rev. B*, 104:054434, 2021.
- [42] S. Vélez, S. Ruiz-Gómez, J. Schaab, E. Gradauskaitė, M. S. Wörnle, P. Welter, B. J. Jacot, C. L. Degen, M. Trassin, M. Fiebig, and P. Gambardella. Current-driven dynamics and ratchet effect of skyrmion bubbles in a ferrimagnetic insulator. *Nature Nanotechnol.*, 17:834–841, 2022.
- [43] A. K. Nayak, V. Kumar, T. Ma, P. Werner, E. Pippel, R. Sahoo, F. Damay, U. K. Roessler, C. Felser, and S. S. P. Parkin. Magnetic antiskyrmions above room temperature in tetragonal Heusler materials. *Nature (London)*, 548(7669):561–566, 2017.
- [44] Siying Huang, Chao Zhou, Gong Chen, Hongyi Shen, Andreas K. Schmid, Kai Liu, and Yizheng Wu. Stabilization and current-induced motion of antiskyrmion in the presence of anisotropic dzyaloshinskii-moriya interaction. *Physical Review B*, 96:144412, 2017.
- [45] M. Hoffmann, B. Zimmermann, G. P. Müller, D. Schürhoff, N. S. Kiselev, C. Melcher, and S. Blügel. Antiskyrmions stabilized at interfaces by anisotropic Dzyaloshinskii-Moriya interactions. *Nature Commun.*, 8:308, 2017.
- [46] A. A. Kovalev and S. Sandhoefner. Skyrmions and antiskyrmions in quasi-two-dimensional magnets. *Front. Phys.*, 6:98, 2018.
- [47] Mariam Hassan, Sabri Koraltan, Aladin Ullrich, Florian Bruckner, Rostyslav O. Serha, Khrystyna V. Levchenko, Gaspere Varvaro, Nikolai S. Kiselev, Michael Heigl, Claas Abert, Dieter Suess, and Manfred Albrecht. Dipolar skyrmions and antiskyrmions of arbitrary topological charge at room temperature. *Nature Physics*, 20:615–622, 2024.
- [48] Kai Huang, Edward Schwartz, Ding-Fu Shao, Alexey A. Kovalev, and Evgeny Y. Tsymbal. Magnetic antiskyrmions in two-dimensional van der Waals magnets engineered by layer stacking. *Physical Review B*, 109:024426, 2024.
- [49] Zhidong He, Zhuolin Li, Zhaohui Chen, Zhan Wang, Jun Shen, Shouguo Wang, Cheng Song, Tongyun Zhao, Jianwang Cai, Shi-Zeng Lin, Ying Zhang, and Baogen Shen. Experimental observation of current-driven antiskyrmion sliding in stripe domains. *Nature Materials*, 23:1048–1054, 2024.
- [50] A. Bogdanov and A. Hubert. The stability of vortex-like structures in uniaxial ferromagnets. *Journal of Magnetism and Magnetic Materials*, 195:182–192, 1999.
- [51] M. Finazzi, M. Savoini, A. R. Khorsand, A. Tsukamoto, A. Itoh, L. Duò, A. Kirilyuk, Th. Rasing, and M. Ezawa. Laser-induced magnetic nanostructures with tunable topological properties. *Physical Review Letters*, 110:177205, 2013.
- [52] Hiroyuki Fujita and Masahiro Sato. Ultrafast generation of skyrmionic defects with vortex beams: Printing laser profiles on magnets. *Physical Review B*, 95:054421, 2017.
- [53] Alexander G. Kolesnikov, Maksim E. Stebliy, Alexander S. Samardak, and Alexey V. Ognev. Skyrmionium – high velocity without the skyrmion hall effect. *Scientific Reports*, 8:16966, 2018.
- [54] S. L. Zhang, W. W. Wang, D. M. Burn, H. Peng, H. Berger, A. Bauer, C. Pfeleiderer, G. van der Laan, and T. Hesjedal. Manipulation of skyrmion motion by magnetic field gradients. *Nature Commun.*, 9:2115, 2018.
- [55] J. Xia, X. Zhang, M. Ezawa, Q. Shao, X. Liu, and Y. Zhou. Dynamics of an elliptical ferromagnetic skyrmion driven by the spin-orbit torque. *Appl. Phys. Lett.*, 116:022407, 2020.
- [56] Yuichi Ishida and Kenji Kondo. Theoretical comparison between skyrmion and skyrmionium motions for spintronics applications. *Japanese Journal of Applied Physics*, 59:SGGI04, 2020.
- [57] R. F. L. Evans. Atomistic Spin Dynamics. In W. Andreoni and S. Yip, editors, *Handbook of Materials Modeling: Applications: Current and Emerging Materials*, pages 1–23. Springer International Publishing, 2018.
- [58] J. Iwasaki, M. Mochizuki, and N. Nagaosa. Universal current-velocity relation of skyrmion motion in chiral magnets. *Nature Commun.*, 4(1):1463, February 2013.
- [59] J. Iwasaki, M. Mochizuki, and N. Nagaosa. Current-induced skyrmion dynamics in constricted geometries. *Nature Nanotechnol.*, 8(10):742–747, October 2013.
- [60] Siying Huang, Chao Zhou, Gong Chen, Hongyi Shen, Andreas K. Schmid, Kai Liu, and Yizheng Wu. Stabilization and current-induced motion of antiskyrmion in the presence of anisotropic dzyaloshinskii-moriya interaction. *Phys. Rev. B*, 96:144412, 2017.
- [61] X. S. Wang, H. Y. Yuan, and X. R. Wang. A theory on skyrmion size. *Communications Physics*, 1(1):31, 2018.
- [62] S. Seki and M. Mochizuki. *Skyrmions in Magnetic Materials*. Springer International Publishing, 2016.
- [63] T. L. Gilbert. A phenomenological theory of damping in ferromagnetic materials. *IEEE Trans. Mag.*, 40(6):3443–3449, 2004.
- [64] See supplemental material for animations showing the textures motion.
- [65] C. Reichhardt, D. Ray, and C. J. Olson Reichhardt. Quantized transport for a skyrmion moving on a two-dimensional periodic substrate. *Phys. Rev. B*, 91:104426, 2015.
- [66] J. Iwasaki, M. Mochizuki, and N. Nagaosa. Universal current-velocity relation of skyrmion motion in chiral

- magnets. *Nature Commun.*, 4:1463, 2013.
- [67] S. L. Zhang, A. Bauer, H. Berger, C. Pfleiderer, G. van der Laan, and T. Hesjedal. Imaging and manipulation of skyrmion lattice domains in  $\text{Cu}_2\text{OSeO}_3$ . *Appl. Phys. Lett.*, 109(19):192406, 2016.
- [68] C. Reichhardt and C. J. Olson Reichhardt. Shapiro steps for skyrmion motion on a washboard potential with longitudinal and transverse ac drives. *Phys. Rev. B*, 92:224432, 2015.
- [69] C.-L. Zhang, J.-N. Wang, C.-K. Song, N. Mehmood, Z.-Z. Zeng, Y.-X. Ma, J.-B. Wang, and Q.-F. Liu. Edge-guided heart-shaped skyrmion. *Rare Metals*, 41:865–870, 2022.
- [70] Jonas Nothhelfer, Sebastián A. Díaz, Stephan Kessler, Tobias Meng, Matteo Rizzi, Kjetil M. D. Hals, and Karin Everschor-Sitte. Steering majorana braiding via skyrmion-vortex pairs: A scalable platform. *Physical Review B*, 105:224509, 2022.